Supporting Information: Quantum Algorithm for Calculating Molecular Vibronic Spectra

Nicolas P. D. Sawaya*

Intel Labs, Santa Clara, California, USA

Joonsuk Huh†

Department of Chemistry, Sungkyunkwan University, Republic of Korea;

SKKU Advanced Institute of Nanotechnology (SAINT),

Sungkyunkwan University, Republic of Korea

(Dated: June 10, 2019)

CONTENTS

S1. HAMILTONIAN CONSTRUCTION

Here we give a more pedagogical summary of the Hamiltonian construction summarized in the main text. The procedure involves these three transformations: $\{\vec{q}_A, \vec{p}_A\} \rightarrow \{\vec{Q}_A, \vec{P}_A\} \rightarrow \{\vec{Q}_B, \vec{P}_B\} \rightarrow \{\vec{q}_B, \vec{p}_B\}$. Mass-weighted position and moment operators, $\vec{Q}_s$ and $\vec{P}_s$ respectively, are [Huh11]

$$\vec{Q}_s = \mathbf{\Omega}_s^{-1} \vec{q_s} \tag{S1}$$

$$\vec{P}_s = \mathbf{\Omega}_s \vec{p_s} \tag{S2}$$

with the $M \times M$ matrix

$$\mathbf{\Omega}_s = diag([\omega_{s1}, ..., \omega_{sM}])^{\frac{1}{2}} \tag{S3}$$

where $\{\omega_{sk}\}$ are the scalar harmonic oscillator frequencies of normal mode k on PES s.

* nicolas.sawaya@intel.com

† joonsukhuh@gmail.com

Because the Duschinsky transformation is not dimensionless, its direct application is appropriate only to the vector of mass-weighted position and momentum operators:

$$\vec{Q}_B = \mathbf{S}\vec{Q}_A + d \tag{S4}$$

$$\vec{P}_B = \mathbf{S}\vec{P}_A. \tag{S5}$$

Then the following are used to obtain the final dimensionless operators:

$$\vec{q}_B = \mathbf{\Omega}_B \vec{Q}_B \tag{S6}$$

$$\vec{p}_B = \mathbf{\Omega}_B^{-1} \vec{P}_B. \tag{S7}$$

Combining these steps leads to equations the following formulas from the main text

$$\vec{q}_B = \mathbf{\Omega}_B \mathbf{S} \mathbf{\Omega}_A^{-1} \vec{q}_A + \mathbf{\Omega}_B \vec{d} \tag{S8}$$

$$\vec{p}_B = \mathbf{\Omega}_B^{-1} \mathbf{S} \mathbf{\Omega}_A \vec{p}_A, \tag{S9}$$

An alternative route for expressing H_B in terms of the operators of PES A (the one taken in references [MF98, HGP+15]) first transforms the ladder operators directly using the transformation

$$\vec{b}^\dagger = \frac{1}{2}(J - (J^t)^{-1})\vec{a} + \frac{1}{2}(J + (J^t)^{-1})\vec{a}^\dagger + \frac{1}{\sqrt{2}}\vec{\delta} \tag{S10}$$

where $\{\hat{a}_i^\dagger\}$ and $\{\hat{b}_i^\dagger\}$ are respectively creation operators for states of PES A and B, and $J = \mathbf{\Omega_B S \Omega_A^{-1}}$. Eq. S10 is then used to construct the Hamiltonian $H_B = \sum_i \omega_{Bi}(b_i^\dagger b_i + \frac{1}{2})$.

It is important to note that there are oftentimes only one or a few electronic transitions that are relevant for a chemist, often the transition between the ground and first excited state. The potential energy surface (PES) of two electronic states must be calculated beforehand, with one of several electronic structure algorithms. For most organic molecules, density functional theory calculations (which roughly speaking often have cubic scaling in

the number of electrons) typically provide electronic PESs that are accurate enough to produce vibronic spectra that match experiment. For other classes of molecules, substantially more expensive methods may be required for obtaining the PES [HJO14].

S2. QHO TO QUBIT MAPPINGS

To implement the algorithm within the standard quantum circuit model, one requires a mapping of quantum harmonic oscillators to a set of qubits. Several mappings from bosonic DOFs to qubits have been proposed in the past [Som05, MSAH18b, MSAH18a, MMS+18]. Here, we outline what are perhaps the two most straightforward mappings for the QHO, which in this work we will call the standard binary and the unary mappings. It is worth mentioning that we would not expect an approach based on the Holstein-Primakoff transformation [HP40] to be particularly promising, since it would require first mapping a bosonic system to a spin-s system, after which one would need the additional step of mapping to spin-half qubits using Clebsch-Gordon coefficients.

Here we summarize how one would convert the operators of H_B into quantum gates of the standard circuit model. The mappings are used to represents operators $\tilde{a}_i^\dagger$ and $\tilde{a}_i$ in qubits.

The *standard binary* mapping represents each level as a binary number such that any integer is represented as $\sum_{p=0}^{p_{max}-1} x_p 2^p$, where p is the qubit id. The state $[|0\rangle, |1\rangle, |2\rangle, |3\rangle, |4\rangle, ...]^T$ is isomorphic to $[|000\rangle, |001\rangle, |010\rangle, |011\rangle, |100\rangle, ...]^T$, where a mapping to 3 qubits was used in this example. Hence each QHO eigenlevel l is a string of 0s and 1s. Any single-mode operator used in constructing Hamiltonian H_B can be expressed in terms of elements $|l\rangle\langle l'|$, where l and l' denote two vibrational levels. In qubit space this leads to operators of the form $|x_0...x_{p_{max}}\rangle\langle x'_0...x'_{p_{max}}|$ where each x_p is a binary value and p_{max} is the number of qubits used in the mapping for a particular mode. As $|x_0...x_{p_{max}}\rangle\langle x'_0...x'_{p_{max}}|$ is equivalent to $|x_0\rangle\langle x'_0| \otimes \ldots \otimes |x_{p_{max}}\rangle\langle x'_{p_{max}}|$, in the latter expression one of four operators is substituted for each single-qubit operator:

$$|0\rangle\langle 1| = \frac{1}{2}(X + iY)[= \sigma^-] \tag{S11}$$

$$|1\rangle\langle 0| = \frac{1}{2}(X - iY)[= \sigma^+] \tag{S12}$$

$$|0\rangle\langle 0| = \frac{1}{2}(1+Z) \tag{S13}$$

$$|1\rangle\langle 1| = \frac{1}{2}(1-Z) \tag{S14}$$

where $\{X, Y, Z\}$ are the Pauli operators, and 1 is the identity operator. In the standard binary mapping, every term $|l'\rangle\langle l|$ leads to a qubit-space operator that operates on all p_{max} qubits.

The less compact *unary* encoding (for which the earliest reference we are aware of is [Som05]) maps $[|0\rangle, |1\rangle, |2\rangle, |3\rangle, |4\rangle, ...]^T$ to $[|00001\rangle, |00010\rangle, |00100\rangle, |01000\rangle, ...]$, requiring more qubits but fewer gates to implement an operator. There are $L_{max} + 1$ qubits in this mapping, as one qubit is reserved for the vacuum state. Though the standard binary mapping utilizes the full Hilbert space, the unary code uses only a small subspace of it. As a result, individual terms of the number operator, i.e. $l|l\rangle\langle l|$, are represented by a single qubit operator using Eq. S14; nearest-level terms like $|l+1\rangle\langle l|$ can be represented by two-qubit operators $\sigma_l^- \sigma_{l+1}^+$.

In real-world implementations, the choice of mapping is likely to depend on a given hardware's qubit count and connectivity. In near-term devices without error correction, the coherence time will have to be considered as well, as different mappings produce circuits of differing depths. Detailed analysis of the cost of each mapping, for a given L_{max}, is deferred to future work, as this requires detailed consideration of circuit optimization, gate cancellations, and qubit connectivity constraints.

The quantum circuit model requires us to set a finite cutoff for the maximum occupation number of each QHO. For vibronic transitions in real molecules, the number l_j of vibrational quanta in the jth mode does not exceed some maximum value $L_{max,j}$ (assuming some finite precision) [JSB07]. In practice, on a future real-world quantum computer, the simplest solution is to increase $L_{max,j}$ values for all modes until convergence is reached.

S3. FINITE TEMPERATURE ALGORITHM

Finite temperature effects can be included by appending additional steps before and after the zero temperature algorithm, in line with previous work [HY17]. The idea is to begin with a purification of the mixed state of the Bolzmann distribution, by having each independent

mode be represented by two subspaces in a purified Fock state. It is necessary to introduce the scalar function $E_A(\mathbf{n})$, defined as the energy of a Fock state in PES A:

$$E_A(\mathbf{n}) = E_A([n_0, ..., n_M]) = \sum_i \omega_i(n_i + \frac{1}{2}), \tag{S15}$$

where n_i is the occupation number of the ith mode.

First we add an additional register, I (for 'initial state'), of ancilla qubits. Registers I and S must have the same size, and we prepare a pure state $|\Psi_{IS}\rangle = \sum |\phi\rangle_I |\psi\rangle_S$ such that $\rho_{th} = Tr_I(|\Psi_{IS}\rangle\langle\Psi_{IS}|)$ is the desired Gibbs thermal state in the initial PES. Before running the QPE routine, we need the pure state

$$|\Psi_{IS}\rangle = \sum_{\mathbf{n}} \kappa_{\mathbf{n}} |\mathbf{n}\rangle_I \otimes |\mathbf{n}\rangle_S = \sum_{\mathbf{n}} \sqrt{\langle\mathbf{n}|\rho_{th}|\mathbf{n}\rangle} |\mathbf{n}\rangle_I \otimes |\mathbf{n}\rangle_S \tag{S16}$$

where $|\mathbf{n}\rangle = |n_0, ..., n_M\rangle$. To prepare $|\Psi_{IS}\rangle = \hat{V}(\beta)|\mathbf{0}\rangle_I|\mathbf{0}\rangle_S$, one implements the unitary operator

$$\hat{V}(\beta) = \bigotimes_i^M \exp(\theta_i(\alpha_i^\dagger a_i^\dagger - \alpha_i a_i)/2) \tag{S17}$$

where $\alpha_i^\dagger$ and α_i are ladder operators for the ith vibrational mode of register I. The inverse temperature is $\beta = 1/k_B T$, where k_B is the Boltzman constant and T is temperature. Angle θ_i is defined by $\tanh(\theta_i/2) = \exp(-\beta\hbar\omega_i/2) = \sqrt{\overline{n}_i/(\overline{n}_i + 1)}$ and $\overline{n}_i$ is the mean quantum number for mode i [MRN+89, HY17]. This operator can be applied using the previously discussed procedure to map arbitrary bosonic operators to qubit operators (Section S2).

After this initial state preparation step, the remainder of the algorithm proceeds as before, but with the following additional elements. After the QPE circuit is applied using registers S and E as before, registers I and E are both measured. The measured state $|\mathbf{n}_I\rangle$ in register I effectively acts as a label, indicating the vibrational eigenstate (Fock state) in the initial PES from which the measured transition occurred. Finally, the contribution to the vibronic spectrum is $\tilde{\varepsilon}_i - E_A(\mathbf{n}_I)$, instead of just $\tilde{\varepsilon}_i$, because the measured transition "began" in vibrational state $|\mathbf{n}_I\rangle$ in the A basis. An outline of the procedure is given in Appendix S4 and a quantum circuit diagram is shown in Fig. 2 (main text). For anharmonic PESs, a similar procedure would be used, with an appropriate anharmonic preparation step used in place of Eq. S17 [Chr04, PW09].

S4. OUTLINE OF ALGORITHMS

What follows is an outline of the zero- and finite-temperature algorithms for calculating molecular vibronic spectra.

Some conceptual clarifications are worth noting. In both the zero- and finite-temperature algorithms, the procedure is to produce a histogram with an arbitrary energy resolution, determined by the number of bits used in quantum register E. Quantum superposition is the key to the algorithm; it removes the need to consider each state explicitly. Even in the finite temperature case, one does not explicitly consider every non-negligible state of the Boltzmann distribution—one prepares a superposition all the possibilities for initial and final states, and then samples their energies. The problem is effectively reduced to sampling from a one-dimensional probability distribution corresponding to the (zero- or finite-temperature) vibronic energy spectrum.

Zero-temperature algorithm:

1. Initialize state $|0\rangle_S|0\rangle_E$.

2. Run QPE using Hamiltonian H_B, expressed in the A basis: $|0\rangle|0\rangle \to \sum_i c_i|\psi_i\rangle|\tilde{\varepsilon}_i\rangle$.

3. Measure register E to obtain eigenenergy $\tilde{\varepsilon}_i$: $\sum_i c_i|\psi_i\rangle|\tilde{\varepsilon}_i\rangle \to A_j \sum_{k\in\mathcal{D}_j} c_k|\psi_k\rangle|\tilde{\varepsilon}_j\rangle$, where A_j is a renormalization constant.

4. If desired, perform additional analysis on the preserved state $A_j \sum_{k\in\mathcal{D}_j} c_k|\psi_k\rangle$ in register S, as discussed in the main text. For example, perform a SWAP test with another state, or resolve one of the Fock states in $\mathcal{D}_j$.

5. Repeat these steps to obtain a histogram of $\tilde{\varepsilon}_i$ values.

Finite-temperature algorithm:

1. Initialize state $|0\rangle_I|0\rangle_S|0\rangle_E$.

2. Prepare the thermal state by acting on registers I and S: $\hat{V}(\beta)|0\rangle|0\rangle|0\rangle \to \sum_{\mathbf{n}} \kappa_{\mathbf{n}}|\mathbf{n}\rangle|\mathbf{n}\rangle|0\rangle$.

3. Apply QPE with H_B, on registers S and E: $\sum_{\mathbf{n}} \kappa_{\mathbf{n}}|\mathbf{n}\rangle|\mathbf{n}\rangle|0\rangle \to \sum_{\mathbf{n}} \kappa_{\mathbf{n}}|\mathbf{n}\rangle \sum_i (c_{\mathbf{n},i}|\psi_i\rangle|\tilde{\varepsilon}_i\rangle)$.

4. Measure both registers E and I: $\to |\mathbf{n}_I\rangle(A_{j,\mathbf{n}_I} \sum_{k\in\mathcal{D}_j} c_{\mathbf{n}_I,k}|\psi_k\rangle)|\tilde{\varepsilon}_j\rangle$.

5. Perform optional analysis on register S, as previously mentioned.

6. The contribution to the histogram is then $\tilde{\varepsilon}_j - E_A(\mathbf{n}_I)$. (Contrast this with the zero-temperature case, where $E_A(\mathbf{n}_I)$ is omitted.)

S5. COMPUTATIONAL SCALING

Below we assume the parameters $\mathbf{S}$, $\vec{\delta}$, $\mathbf{\Omega}_A$, and $\mathbf{\Omega}_B$ are given. Setting aside more advanced linear algebra approaches, both the q-p construction ($H_B = \frac{1}{2}\sum_k^M \omega_{Bk}(q_{Bk}^2 + p_{Bk}^2)$) and the ladder operator construction ($H_B = \sum_i \omega_{Bi}[b_i^\dagger b_i + \frac{1}{2}]$) require $O(M^2)$ classical preparation steps, since all transformations involve only matrix-vector multiplications or diagonal-dense matrix multiplications. For comparison, VBS requires $O(M^3)$ classical steps because it uses the singular value decomposition. As described in the main text, one element of our algorithm uses Hamiltonian simulation to implement H_B for use in the quantum phase estimation (QPE) algorithm. An essential consideration, especially for near- and mid-term hardware, is the computational cost of implementing one Trotter step of the Hamiltonian's propagator.

Each operator b_i is a linear combination of terms in $\{a_i^\dagger\}$ and $\{a_i\}$. The operator H_B, after summing the number operators in $\{b_i^\dagger b_i\}$ and grouping terms, is a linear combination of terms in $\{a_i a_j\}$,$\{a_i^\dagger a_j\}$, $\{a_i a_j^\dagger\}$, and $\{a_i^\dagger a_j^\dagger\}$. Hence in the worst case, the number of terms in H_B scales as $O(M^2)$, meaning the number of operations in a Trotter step is $O(M^2)$ as well.

The circuit depth of a Trotter step scales as $O(M)$, *i.e.* linear-depth. To see this, consider placing two-boson operators (each corresponding to an interaction term such as $a_i^\dagger a_j$) on all boson pairs i, j that satisfy $(i - j) = w \mod N_q$, where $w \in \{1, 2, ..., N_q - 1\}$. For a single value of w, this gate placement has constant depth. Iterating through all values of w yields a circuit with linear depth $O(M)$, and single-boson terms do not change this scaling. The same argument applies to the method based on $\hat{q}$ and $\hat{p}$ operators. Note that the finite-temperature algorithm scales no worse than the zero-temperature procedure, since the state preparation takes $O(M)$ operations with $O(1)$ depth.

When anharmonic effects are included, the complexity of implementing a Trotter step will be $O(M^k)$, where k is the highest-order term in the Taylor expansion of the anharmonic Hamiltonian. It is possible that there will be methods for reducing this complexity in the

anharmonic case, for example by using other other classes of functions in the expansion, *e.g.* the Morse potential.

S6. MOLECULAR DATA

The four simulated molecules, all of the C_{2v} point group, have three vibrational modes: a bending mode, a symmetric stretch, and an anti-symmetric stretch. Due to symmetry, the first two modes are decopuled from the anti-symmetric mode, assuming the harmonic approximation. We consider only the two coupled modes in the harmonic analyses.

For all molecules other than NO_2, we are effectively calculating the photoelectron spectrum, as we are considering an ionization process. Additionally, because of the experimental difficulty in photon counting for higher occupation numbers, in the future it is possible that these molecules might be more easily simulated on a universal quantum computer than a photonic device [CRE+18, SLZ+18]. The electronic transitions are $SO_2^- \rightarrow SO_2 + e^-$ [LYKC09], $H_2O(D_2O) \rightarrow H_2O^+(D_2O^+) + e^-$ [Cha08], and NO_2's ground to excited state transition ${}^2A_1 \rightarrow {}^2B_2$ [Ruh94].

The following parameters were used, taken from the literature. $\mathbf{S}$ and δ are dimensionless; energies of $\vec{\omega}$ are in wavenumbers, cm^{-1}.

$SO_2^- \rightarrow SO_2 + e^-$ [LYKC09]:

$$\mathbf{S}_{SO_2} = \begin{bmatrix} 0.9979 & 0.0646 \\ -0.0646 & 0.9979 \end{bmatrix} \tag{S18}$$

$$\delta_{SO_2} = \begin{bmatrix} -1.8830 \\ 0.4551 \end{bmatrix}$$

$$\vec{\omega}_{SO_2^-} = \begin{bmatrix} 943.3 \\ 464.7 \end{bmatrix}$$

$$\vec{\omega}_{SO_2} = \begin{bmatrix} 1178.1 \\ 518.8 \end{bmatrix}$$

$H_2O \rightarrow H_2O^+ + e^-$ [Cha08]:

$$\mathbf{S}_{H_2O} = \begin{bmatrix} 0.9884 & -0.1523 \\ 0.1523 & 0.9884 \end{bmatrix} \tag{S19}$$

$$\delta_{H_2O} = \begin{bmatrix} 0.5453 \\ 4.2388 \end{bmatrix}$$

$$\vec{\omega}_{H_2O} = \begin{bmatrix} 3862 \\ 1649 \end{bmatrix}$$

$$\vec{\omega}_{H_2O^+} = \begin{bmatrix} 2633 \\ 1620 \end{bmatrix}$$

$D_2O \rightarrow D_2O^+ + e^-$ [Cha08]:

$$\mathbf{S}_{D_2O} = \begin{bmatrix} 0.9848 & -0.1737 \\ 0.1737 & 0.9848 \end{bmatrix} \tag{S20}$$

$$\delta_{D_2O} = \begin{bmatrix} 0.7175 \\ 4.8987 \end{bmatrix}$$

$$\vec{\omega}_{D_2O} = \begin{bmatrix} 2785 \\ 1207 \end{bmatrix}$$

$$\vec{\omega}_{D_2O^+} = \begin{bmatrix} 1915 \\ 1175 \end{bmatrix}$$

$NO_2(^2A_1 \rightarrow {}^2B_2)$ [Ruh94]:

$$\mathbf{S}_{NO_2} = \begin{bmatrix} 0.938 & -0.346 \\ 0.346 & 0.938 \end{bmatrix} \tag{S21}$$

$$\delta_{NO_2} = \begin{bmatrix} -4.0419 \\ 5.3185 \end{bmatrix}$$

$$\vec{\omega}_{NO_2(gr)} = \begin{bmatrix} 1358 \\ 757 \end{bmatrix}$$

$$\vec{\omega}_{NO_2(ex)} = \begin{bmatrix} 1461 \\ 739 \end{bmatrix}$$

For our anharmonic simulation, we used the same Duschinsky matrix as before [LYKC09], but used the anharmonic PES for the electrically neutral SO_2 from Smith et al. [SLN84].

We use a harmonic potential energy surface only for the initial PES $SO_2{}^-$, which is a good approximation because the initial vibrational state is in the ground state (Fock vacuum state) of $SO_2{}^-$, *i.e.* the initial state is at the bottom of the PES, where the harmonic approximation is valid. Additionally, the third vibrational mode can no longer be considered decoupled when anharmonic effects are included, making this a simulation of all three vibrational modes. Hence, for the anharmonic spectrum, the following parameters are taken from Lee et al. [LYKC09]:

$$\mathbf{S}_{SO_2^- \to SO_2} = \begin{bmatrix} 0.9979 & 0.0646 & 0 \\ -0.0646 & 0.9979 & 0 \\ 0 & 0 & 1 \end{bmatrix} \tag{S22}$$

$$\delta_{SO_2^- \to SO_2} = \begin{bmatrix} -1.8830 \\ 0.4551 \\ 0 \end{bmatrix} \tag{S23}$$

$$\vec{\omega}_{SO_2^-} = \begin{bmatrix} 943.3 \\ 464.7 \\ 1138.6 \end{bmatrix} \tag{S24}$$

And from Smith et al. [SLN84]:

$$\vec{\omega}_{SO_2}^{anharm} = \begin{bmatrix} 1171 \\ 525 \\ 1378 \end{bmatrix} \tag{S25}$$

We then include the third- and fourth-order terms in the Taylor expansion (Eq. 8 in the main text). Table I gives the coefficients for the anharmonic terms $q_1q_1q_1$, $q_1q_1q_2$, $q_1q_2q_2$, $q_1q_3q_3$, $q_2q_2q_2$, $q_2q_3q_3$, $q_1q_1q_1q_1$, $q_1q_1q_2q_2$, $q_1q_1q_3q_3$, $q_2q_2q_2q_2$, $q_2q_2q_3q_3$, and $q_3q_3q_3q_3$. All of these operators may be mapped to qubit-based Pauli operators using exactly the same procedure that was outlined before (Section S2).

S7. ERROR ANALYSIS

We studied truncation errors, i.e. those due to insufficiently large L_{max}, primarily because this type of error is not present in standard classical vibronic simulations, which are not based

k_{111}	k_{112}	k_{122}	k_{133}	k_{222}	k_{233}	k_{1111}	k_{1122}	k_{1133}	k_{2222}	k_{2233}	k_{3333}
44	-19	-12	159	-7.0	4.7	1.8	-3.1	15	-1.4	-6.5	3.0

TABLE I. Higher-order terms used in the *anharmonic* potential energy surface of the neutral SO_2 molecule [SLN84]. All values are in units of cm^{-1}.

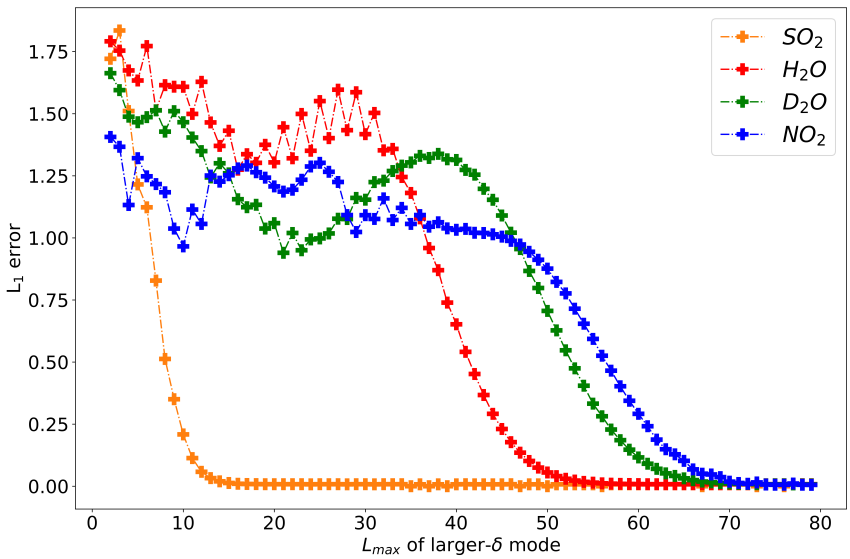

FIG. 1. L_1-norm errors between exact and approximate vibronic spectra, for molecules SO_2, H_2O, D_2O, and NO_2 (where D is deuterium), where each eigenvalue was broadened with a Gaussian of width 100 cm^{-1} to make error analysis possible (broadening is performed after the histogram is constructed). H_2O, D_2O, and NO_2 were chosen because they have particularly high phonon occupation numbers, necessitating a large QHO cutoff L_{max}. In general a larger displacement δ leads to a larger required cutoff. In this simulation, the mode with a smaller δ was assigned a converged L_{max}; hence we isolated the effects of the variable of the more significant (larger δ) mode by varying its L_{max}.

on diagonalizing H_B [RR00, JSB07, BBBS09, Huh11]. All results are obtained by creating H_B with truncated ladder operators, diagonalizing the Hamiltonian, calculating FCFs, and binning the results in bins of width 1 cm^{-1}.

To make our error analysis method possible, the spectra in this work were broadened with a Gaussian of width 100 cm^{-1}, a width that represents $\lesssim 1\%$ of the spectral range

for these four molecules. The broadening is a distinct separate step, and is performed after formation of the histogram. Errors were calculated using the L_1 norm between the exact and approximate spectra (both broadened),

$$\epsilon_{L1} = \int |FCP_{exact}(\omega) - FCP_{approx}(\omega)| d\omega. \tag{S26}$$

Because FCF profiles have unit norm, the worst case of two spectra with zero overlap yields $\epsilon_{L1} = 2$.

The exact and approximate Hamiltonians were constructed using equation S10, varying ladder operator size to reflect L_{max}. The numerically exact results were considered converged when the L_1 norm between two subsequent L_{max} values was below 10^{-4}. We validated our method's numerically exact results by demonstrating that our results for SO_2 were identical to those produced by the software program hotFCHT [BFK98], which uses an entirely different algorithmic approach based on recurrence formulas.

For all simulations, the mode that required a smaller cutoff was set to a high converged value, so that we isolated the effect of L_{max} for the mode requiring a larger cutoff. This is the mode that is more shifted, i.e. the one with larger $|\delta|$. Hence for SO_2 we varied the cutoff for the first mode, while for the other three molecules we varied the cutoff for the second mode. We plotted the approximate spectra (dotted lines, Fig. 3) in order to demonstrate the qualitative effect of an insufficient cutoff. The approximate spectra in Fig. 3 were arbitrarily chosen such that ϵ_{L1} lies between 0.2 and 0.25. For these illustrative approximate spectra, ϵ_{L1} and L_{max} are $\{0.208, 0.231, 0.228, 0.241\}$ and $\{10, 45, 57, 61\}$ for SO_2, H_2O, D_2O, and NO_2, respectively.

Qualitatively, the effect of a too-low cutoff number is to preferentially blue shift the higher energy peaks (Fig. 3 in main text). This numerical artifact results from the fact that the L_{max} cutoff effectively introduces anharmonicity to the problem; operators constructed from exact (infinite) ladder operators will not have the same spectrum as those constructed from truncated operators. As L_{max} is increased, the low energy peaks are converged much sooner than the high energy peaks are. For instance, in the approximate H_2O spectrum shown, there is an effectively perfect match below $\sim$15,000 cm^{-1}, but the blue-shift errors become even larger than $\sim$100 cm^{-1} for eigenvalues above $\sim$23,000 cm^{-1}. Being aware of this consistent qualitative error behavior can provide guidance when interpreting results from an implementation of our quantum algorithm. Additional results on convergence with

increasing L_{max} are shown in Section S7. When using a future quantum computer, one would need to run the algorithm with increasing L_{max} until the spectrum is converged.

Fig. 1 shows ϵ_{L1} as a function of L_{max}, again for the mode with larger δ. The approximate L_{max} cutoffs at which the error can be considered converged are [12, 51, 64, 69] respectively for SO_2, H_2O, D_2O, and NO_2. For this small set, the L_{max} order matches the order of increasing δ, which is the expected approximate trend. Using the standard binary mapping for QHO levels (which requires $\lceil \log_2 L_{max} \rceil$ for a given mode) would mean that the number of qubits required for the larger-δ mode are 4, 6, 6, and 7 qubits, respectively.

Counter-intuitively, L_{max} must be substantially larger than the highest QHO level at which appreciable intensity exists. For example, one may naively expect that L_{max}=8 would be sufficient for SO_2, since the FC factor $\sum_{n'_1} |\langle \mathbf{0}|n'_0 = 8\rangle|^2$ is a near-negligible value of $\sim 1.6 \times 10^{-3}$ (just 0.6% of the largest FCF). But L_{max}=13 is required for eigenvalue positions and the L_1-norm error to converge. This is despite the fact that transitions to levels 12 and 13 are very small, with $\sum_{n'_1} |\langle \mathbf{0}|n'_0 = 12\rangle|^2 \approx 5.2 \times 10^{-5}$ and $\sum_{n'_1} |\langle \mathbf{0}|n'_0 = 13\rangle|^2 \approx 1.5 \times 10^{-5}$.

The truncation values are not expected to depend explicitly on M because the intensities of a given mode's vibronic progression is known to approximately follow the rapidly-decaying Poisson distribution [MK08].

[BBBS09] Vincenzo Barone, Julien Bloino, Malgorzata Biczysko, and Fabrizio Santoro. Fully integrated approach to compute vibrationally resolved optical spectra: From small molecules to macrosystems. *Journal of Chemical Theory and Computation*, 5(3):540–554, Mar 2009.

[BFK98] R. Berger, C. Fischer, and M. Klessinger. Calculation of the vibronic fine structure in electronic spectra at higher temperatures. 1. Benzene and pyrazine. *The Journal of Physical Chemistry A*, 102(36):7157–7167, Sep 1998.

[Cha08] Jia-Lin Chang. A new method to calculate Franck-Condon factors of multidimensional harmonic oscillators including the Duschinsky effect. *The Journal of Chemical Physics*, 128(17):174111, May 2008.

[Chr04] Ove Christiansen. A second quantization formulation of multimode dynamics. *The Journal of Chemical Physics*, 120(5):2140–2148, feb 2004.

[CRE+18] William R Clements, Jelmer J Renema, Andreas Eckstein, Antonio A Valido, Adriana

Lita, Thomas Gerrits, Sae Woo Nam, W Steven Kolthammer, Joonsuk Huh, and Ian A Walmsley. Approximating vibronic spectroscopy with imperfect quantum optics. *Journal of Physics B: Atomic, Molecular and Optical Physics*, 51(24):245503, Nov 2018.

[HGP+15] Joonsuk Huh, Gian Giacomo Guerreschi, Borja Peropadre, Jarrod R. Mcclean, and Alán Aspuru-Guzik. Boson sampling for molecular vibronic spectra. *Nature Photonics*, 9(9):615–620, 2015.

[HJO14] Trygve Helgaker, Poul Jorgensen, and Jeppe Olsen. *Molecular Electronic-Structure Theory.* John Wiley and Sons, Ltd, 2014.

[HP40] T. Holstein and H. Primakoff. Field dependence of the intrinsic domain magnetization of a ferromagnet. *Phys. Rev.*, 58:1098–1113, Dec 1940.

[Huh11] Joonsuk Huh. *Unified Description of Vibronic Transitions with Coherent States.* PhD thesis, Goethe Univ. Frankfurt, 2011.

[HY17] Joonsuk Huh and Man-Hong Yung. Vibronic boson sampling: Generalized gaussian boson sampling for molecular vibronic spectra at finite temperature. *Scientific Reports*, 7(1):7462, Aug 2017.

[JSB07] H.-C. Jankowiak, J. L. Stuber, and R. Berger. Vibronic transitions in large molecular systems: Rigorous prescreening conditions for Franck–Condon factors. *The Journal of Chemical Physics*, 127(23):234101, Dec 2007.

[LYKC09] Cheng-Luen Lee, Sin-Hua Yang, San-Yu Kuo, and Jia-Lin Chang. A general formula of two-dimensional Franck-Condon integral and the photoelectron spectroscopy of sulfur dioxide. *Journal of Molecular Spectroscopy*, 256(2):279–286, Aug 2009.

[MF98] P.-A. Malmqvist and N. Forsberg. Franck-Condon factors for multidimensional harmonic oscillators. *Chemical Physics*, 228(1-3):227–240, Mar 1998.

[MK08] Volkhard May and Oliver Kuhn. *Charge and Energy Transfer Dynamics in Molecular Systems.* John Wiley and Sons, 2008.

[MMS+18] Sam McArdle, Alex Mayorov, Xiao Shan, Simon Benjamin, and Xiao Yuan. Quantum computation of molecular vibrations, 2018.

[MRN+89] A. Mann, M. Revzen, K. Nakamura, H. Umezawa, and Y. Yamanaka. Coherent and thermal coherent state. *Journal of Mathematical Physics*, 30(12):2883–2890, Dec 1989.

[MSAH18a] Alexandru Macridin, Panagiotis Spentzouris, James Amundson, and Roni Harnik. Digital quantum computation of fermion-boson interacting systems. *Phys. Rev. A*, 98:042312,

Oct 2018.

[MSAH18b] Alexandru Macridin, Panagiotis Spentzouris, James Amundson, and Roni Harnik. Electron-phonon systems on a universal quantum computer. *Phys. Rev. Lett.*, 121:110504, Sep 2018.

[PW09] David Poulin and Pawel Wocjan. Sampling from the thermal quantum gibbs state and evaluating partition functions with a quantum computer. *Physical Review Letters*, 103(22):220502, Nov 2009.

[RR00] Peder Thusgaard Ruhoff and Mark A. Ratner. Algorithms for computing Franck-Condon overlap integrals. *International Journal of Quantum Chemistry*, 77(1):383–392, 2000.

[Ruh94] Peder Thusgaard Ruhoff. Recursion relations for multi-dimensional Franck-Condon overlap integrals. *Chemical Physics*, 186(2-3):355–374, Sep 1994.

[SLN84] A.D. Smith, W.-K. Liu, and D.W. Noid. Vibrational levels of triatomic molecules - semi-classical self-consistent-field and classical spectral calculations. *Chemical Physics*, 89(3):345–351, oct 1984.

[SLZ+18] Yangchao Shen, Yao Lu, Kuan Zhang, Junhua Zhang, Shuaining Zhang, Joonsuk Huh, and Kihwan Kim. Quantum optical emulation of molecular vibronic spectroscopy using a trapped-ion device. *Chemical Science*, 9(4):836–840, 2018.

[Som05] Rolando D. Somma. Thesis: Quantum computation, complexity, and many-body physics, 2005.